



HAL
open science

Multiple-beam Interference Spectroscopy: Instrument Analysis and Spectrum Reconstruction

Mohamad Jouni, Daniele Picone, Mauro Dalla Mura

► **To cite this version:**

Mohamad Jouni, Daniele Picone, Mauro Dalla Mura. Multiple-beam Interference Spectroscopy: Instrument Analysis and Spectrum Reconstruction. 2024. hal-04666929v2

HAL Id: hal-04666929




<https://hal.science/hal-04666929v2>

Preprint submitted on 13 Oct 2024 (v2), last revised 17 Oct 2024 (v3)

HAL is a multi-disciplinary open access archive for the deposit and dissemination of scientific research documents, whether they are published or not. The documents may come from teaching and research institutions in France or abroad, or from public or private research centers.

L'archive ouverte pluridisciplinaire **HAL**, est destinée au dépôt et à la diffusion de documents scientifiques de niveau recherche, publiés ou non, émanant des établissements d'enseignement et de recherche français ou étrangers, des laboratoires publics ou privés.

Multiple-beam Interference Spectroscopy: Instrument Analysis and Spectrum Reconstruction

Mohamad Jouni , *Member, IEEE*, Daniele Picone , *Member, IEEE*, Mauro Dalla Mura , *Senior Member, IEEE*

Abstract—Hyperspectral imaging systems based on multiple-beam interference (MBI), such as Fabry-Perot interferometry, are attracting interest due to their compact design, high throughput, and fine resolution. However, unlike dispersive devices, the desired spectra in interferometric devices are reconstructed from the measured interferograms. Although the response function of MBI devices is modeled by the Airy function, existing reconstruction techniques are often constrained to the Fourier-transform spectroscopy, which is tailored for two-beam interference (TBI). Those approaches pose limitations for MBI and are susceptible to non-idealities like irregular sampling and noise. To address these challenges, we propose to use inversion techniques with prior knowledge that rely on a transfer matrix that embeds more accurately the real-world conditions of the device in the theoretical model, for which we also propose an analysis of the discretization of the continuous model and the ill-posedness of the problem. We frame our proposed solution as a unified formulation of both MBI and TBI spectroscopy, smoothly transitioning from the classical physical interpretation to a numerical system analysis of this forward matrix representation. Consequently, we extend the range of existing solutions for spectrum reconstruction, framing them as a classic optimization problem. Specifically, we employ a Bayesian framework incorporating prior knowledge, such as sparsity constraints. Experiments on simulated and real data demonstrate the framework’s flexibility and noise robustness compared to conventional algorithms. An implementation of the code is available at <https://github.com/mhmdjouni/inverspyctrometry>.

Index Terms—Interferometry, spectroscopy, numerical analysis, inverse problems, variational reconstruction.

I. INTRODUCTION

MEASURING the *spectrum* of a light source in a scene is at the core of imaging spectroscopy and has deep implications in various fields, such as geology, gas detection, security, remote sensing, disaster prevention, and more [1], [2], [3], [4]. In recent times, both the scientific community and

Manuscript received DD Month 202Y; revised DD Month 202Y and DD Month 202Y; accepted DD Month 202Y. Date of publication DD Month 202Y; date of current version DD Month 202Y. This work was supported partly by the AuRA region and FEDER under the project ImSPOC-UV (convention FEDER n. RA0022348) by Grant ANR FuMultiSPOC (ANR-20-ASTR-0006), and under project “Pack Ambition International 2021” by Grant 21-007356-01FONC and Grant 21-007356-02INV. (*Corresponding author: Mauro Dalla Mura.*)

Mohamad Jouni and Daniele Picone are with the Centre National de la Recherche Scientifique (CNRS), Grenoble Institute of Technology (Grenoble INP), Grenoble Images Speech Signals and Automatics Laboratory (GIPSA-Lab), Université Grenoble Alpes, 38000 Grenoble, France (e-mail: mohamad.jouni@grenoble-inp.fr; daniele.picone@grenoble-inp.fr).

Mauro Dalla Mura is with CNRS, Grenoble INP, GIPSA-Lab, Université Grenoble Alpes, 38000 Grenoble, France, and also with the Institut Universitaire de France (IUF), 75231 Paris, France (e-mail: mauro.dalla-mura@grenoble-inp.fr).

Digital Object Identifier XXXX/YYYY

industrial venues have shown interest in image spectrometers based on the principle of *interferometry* [5], [6], [7], [8], which is a fundamental tool in domains such as in optics [9], [10], [11], radar [12], radio astronomy [13], among other measurement systems [14], [15], [16]. Compared to dispersive spectrometers, they allow for improved SNR [17], compact instruments with reduced cost [18], and acquisitions with finer spectral resolution [19].

Interferometers are devices that measure the intensity of the interference of superimposed coherent light beams after traveling different optical paths, whose difference is known as the optical path difference (OPD). As such, the spectrum of a point source is collected in a transformed domain, across different OPDs, resulting in the so-called *interferogram*. Since the desired spectra are not immediately intelligible to the final user, the acquired interferograms need to be processed [20], [21]. Fig. 1 illustrates this concept. The two main phenomena of interference are the *two-beam interference (TBI)* and the *multiple-beam interference (MBI)* [5], [6].

Devices based on TBI, such as the Michelson interferometer, are widely employed in spectroscopy. This class of devices belongs to Fourier-transform spectroscopy (FTS) [22], where the acquisition model at a given OPD is expressed as the Fourier transform of the incident spectrum, so the retrieval of the spectrum from an interferogram boils down to a Fourier inversion, i.e. an inverse discrete Fourier transform (IDFT).

For devices based on MBI, the acquisition is described through a superimposition of a potentially infinite number of coherent light waves [5], [6]. The response function of such devices at a given OPD is modeled as an *Airy function*, and it can easily be shown that its Fourier series expansion is composed by harmonics that decay exponentially according to the reflectivity of the interferometer [23]. Recently, MBI devices, especially based on the Fabry-Perot interferometer (FPI), have become preferable for imaging spectroscopy as they are easier to construct, provide finer spectral resolution with more compact designs [24], are less influenced by environmental disturbances [25], and offer higher optical throughput [26]. Fig. 2 illustrates the operating principle of a Michelson interferometer and a FPI.

A. Related Works and Limitations

Traditionally, the properties of MBI interferometers have been used for detecting emission lines and filtering absorption lines in incident light [27]. More recently, some imaging designs and prototypes based on the FPI have been proposed

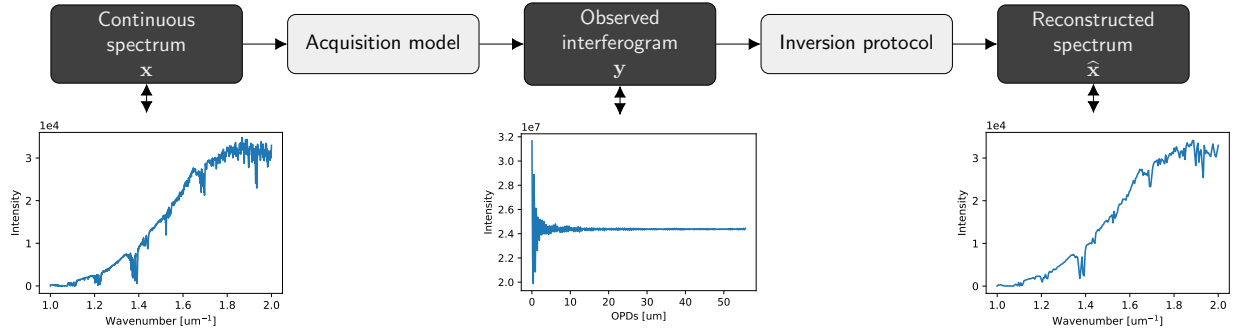


Fig. 1. The acquisition and inversion pipelines of the reconstruction of spectra from interferograms. It portrays both the role of the instrument for capturing the interferogram, which is modeled by a mathematical transformation of the input, and the necessity of an inversion pipeline for spectral reconstruction.

to operate as spectrometers and aim for the full spectrum reconstruction of the incident light. Such devices typically operate in very low reflectivity regimes in order to emulate the operating principle of the standard FTS [28]. For example, different scanning-based devices have been proposed that obtain recordings at different OPDs by adjusting the thickness of the FPI. Among these, some operate in the ultraviolet to near-infrared domains [29], [30], other ones in the thermal range [31], and others with hybrid designs [32], [33]. In [18], a snapshot device has been proposed, featuring a multi-aperture design. The device consists of an array of FPIs with different thicknesses arranged in a staircase pattern, enabling the simultaneous acquisition of recordings at different OPDs.

For most of these devices, the companion techniques proposed for spectrum reconstruction are based on the IDFT. This strategy has however several limitations in terms of accuracy.

In particular, this solution is only valid for MBI-based devices when the intensity of the harmonics is actually negligible, which is not true in most practical scenarios. An often overlooked side-effect of harmonics is their spectral overlapping within the spectral range of interest. IDFT-based techniques are particularly sensitive to this issue, causing important distortions in the reconstruction samples. An analytical solution to address this issue has been proposed in [34], where the discrete Fourier transform (DFT) of the interferogram is expanded using a Haar function. However, this solution is only valid if the reflectivity of the instrument is assumed constant over the spectral range. This challenge becomes even more relevant with multi-aperture snapshot devices [18] where the FPIs may exhibit slightly or very different physical or manufacturing characteristics (e.g., gain, reflectivity).

Moreover, the spectral resolution of DFT-based solutions is strictly limited by the Nyquist-Shannon sampling theorem [35] (hereafter referred to as the *sampling theorem*) and ignore the potential to exploit the contribution of the aliased non-zero spectral samples due to the harmonics that can be potentially collected outside of the spectral range of the instrument.

Finally, the acquired interferogram in most practical applications is irregularly sampled. This is due to the OPDs being associated to physical components of the device, which are in turn sensitive to manufacturing defects. As a result, some distortions occur in the reconstruction, as DFT-based techniques assume that the interferogram is regularly sampled.

B. Contributions

To accommodate these challenges, we propose to use a Bayesian formulation [36], [37] of the problem with a more accurate representation and a numerical analysis of the physical acquisition model. Specifically, a transfer matrix is generated from an Airy function that embeds the physical design conditions of a given MBI-based device, accommodating the challenging case of multi-aperture snapshot devices, and the reconstruction is carried out as a linear inverse problem, incorporating prior information. Since the interferometric model exhibits a domain transform that is related to the Fourier transform, we perform an analysis of the discretization of the continuous model [38], [39] and the well-posedness of the problem in terms of Hadamard [40].

With that goal in mind, the novelty lies in setting a framework for the analysis and resolution of spectrum reconstruction from interferometric measurements, as detailed below. As an extension to our preliminary results in [41], [42]:

- 1) For the acquisition model analysis, we extend the findings of the MBI theoretical model in [19] with a numerical analysis on its discretized version, i.e., the transfer matrix. In particular, we investigate the conditions of well-posedness of the problem in terms of Hadamard [40] under the textbook formulation of both TBI and MBI acquisition systems. First, we summarize the conditions for the proper discretization of the continuous interferometric transformation, and formulate the two regimes in terms of the discrete cosine transform (DCT). Then, we formalize the limitations of spectrum reconstruction in terms of spectral resolution, recoverability, and Hadamard well-posedness.
- 2) For the reconstruction of spectra, first, we represent the model with a transfer matrix that embeds information of real acquisition scenarios such as irregular sampling, variable reflectivity, harmonic contribution, and measurement noise. Then, by using the matrix within a Bayesian framework, we extend the techniques of spectrum reconstruction to linear inverse problems and incorporate prior knowledge such as LASSO [36]. For that, we provide a pedagogical progressive analysis of the ability of these techniques to tackle the non idealities from more specific to more general scenarios.

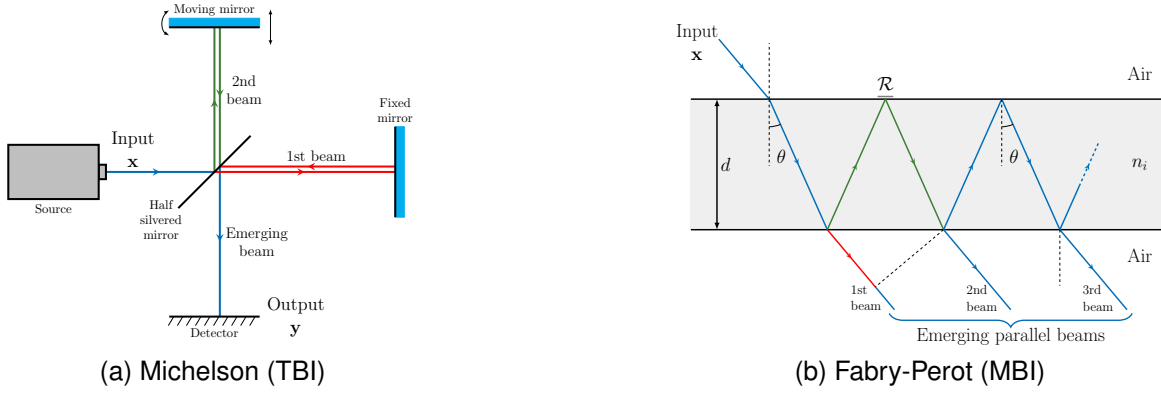


Fig. 2. Illustration of the operation principle of a Michelson interferometer (left) and a Fabry-Perot interferometer (right).

With this analysis, our aim is to establish a novel unified framework that accommodates both TBI and MBI systems, which is missing in the respective literature. Under this umbrella, we are able to describe instruments with different operating principles, reflectivity regimes, physical conditions, and prior information.

The remainder is organized as follows. Section II presents a physical background of TBI and MBI. Section III presents the analysis of the system. Section IV talks about spectrum reconstruction. Sections V and VI present the experiments and results. Finally, a conclusion is drawn in Section VII.

II. ACQUISITION (INSTRUMENTAL) MODEL

In this section, we recall the physical principles behind TBI and MBI. The goal is to describe the acquisition model of the two phenomena throughout the mathematical expression which describes the transformation from the incident light (optical part) to the measured signal (observation part). In the following, the input is described as the continuous spectral radiance of the incident light, while the observation is defined by the resulting discrete interferogram [5], [6].

A. Interferogram Formation

Let us denote the interferogram signal $y(\delta)$ as a function in the domain of the OPDs δ , and the spectrum $x(\sigma)$ as a function in the domain of the wavenumbers σ . Throughout this paper, we use the wavenumbers, defined as the reciprocal of the wavelengths, as they are more convenient and more widespread in the literature of FTS and MBI. For consistency throughout this paper, we express the OPDs δ and wavenumbers σ in μm and μm^{-1} , respectively.

In the following, we assume that the device operates in the arbitrary spectral support $\Omega = [\sigma_{\min}, \sigma_{\max}]$ (where $0 < \sigma_{\min} < \sigma_{\max}$). We also assume that the device is capable of generating a certain fixed OPD δ . The specific mechanisms for generating this OPD will be detailed when relevant.

With this formalism, the interferogram $y(\delta)$ can be modeled by the following equation [5], [6]:

$$y(\delta) = \int_{\Omega} A(\delta, \sigma) x(\sigma) d\sigma, \quad (1)$$

where $A(\delta, \sigma)$ defines the *response function* of the device. In the context of interferometry, one can interpret $A(\delta, \sigma)$ as a domain transfer function from the wavenumbers to the OPDs.

The interferometric response function $A(\delta, \sigma)$ represents the intensity ratio of light interference as a function of σ for each δ [5], [6]. In the following sections, we present the expressions of the response functions for the TBI and MBI. These expressions are described in the context of their most common applications, namely the Michelson interferometer and FPI respectively. However, the reader can consider the described results without loss of generality, as they could be extended without much effort to other use cases as well.

B. Two-beam Interference (TBI)

In a Michelson interferometer, the incident light is split into two beams, which then travel different optical paths d_1 and d_2 until they get reflected by their respective mirrors, before meeting at one point at the detector. Their OPD $\delta = d_1 - d_2$ causes a phase difference $\Delta\phi = 2\pi\delta\sigma$ among the two beams. By adjusting the relative position of one of the mirrors, the OPD can be varied, which allows to study the interference patterns for different phase differences [5], [6].

The response function $A(\delta, \sigma)$ is then defined as the ratio between the captured optical intensity (given by the two beams) and the input intensity $x(\sigma)$, yielding [5], [6]:

$$A(\delta, \sigma) = 2\mathcal{T}(\sigma)(1 + \cos(2\pi\delta\sigma)), \quad (2)$$

where $\mathcal{T}(\sigma) \in [0, 1]$ denotes the transmittance of the Michelson interferometer. The multiplicative factor 2 appears in order to compensate the optical energy in the special case where the beams are evenly split.

For simplicity, by setting $\mathcal{Q}(\sigma) = 2\mathcal{T}(\sigma)$, the observed interferogram $y(\delta)$ is obtained from (1) as follows:

$$\begin{aligned} y(\delta) &= \int_{\Omega} \mathcal{Q}(\sigma) x(\sigma) d\sigma + \int_{\Omega} \mathcal{Q}(\sigma) x(\sigma) \cos(2\pi\delta\sigma) d\sigma \\ &= \mathcal{F}_c\{\mathcal{Q}x\}(0) + \mathcal{F}_c\{\mathcal{Q}x\}(\delta), \end{aligned} \quad (3)$$

where $\mathcal{F}_c\{\mathcal{Q}x\}(\delta)$ represents the *Fourier cosine transform* of the spectral distribution $\mathcal{Q}(\sigma)x(\sigma)$ evaluated in δ . Its expression for $\delta = 0$, namely $\mathcal{F}_c\{\mathcal{Q}x\}(0) = \frac{1}{2}y(0)$, can be expressed as a function of the detected intensity $y(0)$ in the case the beams travel equal paths. Eq. (3) serves as the historical foundation of the term Fourier-transform spectroscopy.

C. Multiple-beam Interference (MBI)

The design of an FPI is typically manufactured using interferometric cavities. Geometrically, a cavity is described as two parallel surfaces separated by a thickness d , which encloses a homogeneous optical material with a refractive index n_i . The overall cavity exhibits a transmittance $\mathcal{T}(\sigma)$ and reflectivity $\mathcal{R}(\sigma) \in [0, 1]$. The incident light is transmitted through the first surface at an angle θ into the interior of the plate, where it gets reflected back and forth between the two surfaces, and attenuated by the reflectivity $\mathcal{R}(\sigma)$ every time it bounces over the cavity surface. After each round trip within the cavity, a beam emerges out of the FPI. These potentially infinite emerging parallel beams are collected at a detector, exhibiting an OPD $\delta = 2n_i d \cos(\theta)$ and a phase difference $\Delta\phi = 2\pi\delta\sigma$ between two consecutive beams [5], [6].

It can be shown [5], [6] that the response function of the FPI can be expressed as the following closed form:

$$A(\delta, \sigma) = \frac{\mathcal{T}^2(\sigma)}{1 + \mathcal{R}^2(\sigma) - 2\mathcal{R}(\sigma) \cos(2\pi\delta\sigma)}, \quad (4)$$

which is widely known as the Airy function. Equivalently, imposing $\mathcal{Q}(\sigma) = \frac{\mathcal{T}^2(\sigma)}{1 - \mathcal{R}^2(\sigma)}$ for simplicity, eq. (4) can be expanded as a Fourier series [19]:

$$\begin{aligned} A(\delta, \sigma) &= \mathcal{Q}(\sigma) \left[1 + 2 \sum_{n=1}^{\infty} \mathcal{R}^n(\sigma) \cos(2\pi n\delta\sigma) \right] \\ &= C_0(\sigma) + \sum_{n=1}^{\infty} C_n(\sigma) \cos(2\pi n\delta\sigma), \end{aligned} \quad (5)$$

where $C_n(\sigma) \forall n \in \mathbb{N}$ are the coefficients such that:

$$C_0(\sigma) = \mathcal{Q}(\sigma); \quad C_n(\sigma) = 2\mathcal{Q}(\sigma)\mathcal{R}^n(\sigma), \quad \forall n \geq 1. \quad (6)$$

Compared to TBI, for each OPD δ , there is a potential harmonic contribution coming from the oscillations $n\delta \forall n \geq 2$. Since the harmonics decay exponentially as $n \rightarrow \infty$, then the model can be approximated as:

$$A(\delta, \sigma) = \sum_{n=0}^{N-1} C_n(\sigma) \cos(2\pi n\delta\sigma) + \mathcal{O}(N), \quad (7)$$

where $\mathcal{O}(N) \approx 0$ includes all the terms associated to more than N reflections, which are negligible as the coefficients $C_n(\sigma)$ become negligible for $n \geq N$. The corresponding interferogram is expressed as follows:

$$y(\delta) = \mathcal{F}_c\{\mathcal{Q}x\}(0) + 2 \sum_{n=1}^{N-1} \mathcal{F}_c\{\mathcal{Q}\mathcal{R}^n x\}(n\delta). \quad (8)$$

Here, each record $y(\delta)$ contains the contribution of not only the fundamental term, but also that of its harmonics.

When the reflectivity $\mathcal{R}(\sigma)$ is too low such that $C_2(\sigma)$ becomes negligible, eq. (8) boils down to the fundamental terms as follows:

$$y(\delta) = \mathcal{F}_c\{\mathcal{Q}x\}(0) + 2\mathcal{F}_c\{\mathcal{Q}\mathcal{R}x\}(\delta). \quad (9)$$

Since $\mathcal{R}(\sigma)$ is assumed very small, one could approximate the term $\mathcal{F}_c\{\mathcal{Q}x\}(0)$ to the mean value of the interferogram, and eq. (9) becomes roughly similar to eq. (3) up to the multiplicative factor $\mathcal{R}(\sigma)$.

III. TRANSFER MATRIX NUMERICAL ANALYSIS

In this section, we aim to derive a proper discrete version of the direct model that describes the acquisition system. The motivation for this is twofold: first, in the OPD domain, we must ensure that the number of acquisitions is finite; second, in the wavenumber domain, we need to sample the continuous range to allow for numerical computations. To this end, we discretize the response function $A(\delta, \sigma)$, defining its sampled version as the transfer matrix in Section III-A.

Additionally, when treated as a linear inverse problem, spectrum reconstruction can be ill-posed or ill-conditioned in terms of Hadamard [40], leading to solutions that are either not unique or unstable. To formalize the nature of the inverse problem at hand, we perform a numerical analysis on the characteristics of the transfer matrix.

First, we start with a brief sampling analysis of the response function in Section III-B [19], [35]. In Section III-C we propose a formalization of the textbook models of TBI and MBI in terms of the DCT-II. A naive reconstruction procedure involves manipulating this result, which ultimately requires the use of the inverse discrete cosine transform (IDCT). However, such procedure exhibits some limitations for the MBI case in terms of spectral resolution. In Section III-D, we give a summary of such limitations [19].

Alternatively, one may also approach the reconstruction problem as *least square* solution, which instead involves a Moore-Penrose inversion of the transfer matrix. In Section III-E, we propose to examine this approach in terms of the condition number of the transfer matrix. We specifically highlight how the system's physical parameters affect this condition number and emphasize the need for regularization even in the ideal textbook MBI scenario.

While sections III-A, III-B, and III-D are derived from the literature, we streamline the findings with practical insights on the algebraic characteristics of the corresponding transfer matrix. These conclusions are utilised to derive our proposed extended analysis in sections III-C and III-E.

A. Transfer Matrix Representation

The discrete representation of the response function is obtained by sampling the wavenumbers domain into K points $\sigma \in \{\sigma_0, \dots, \sigma_{K-1}\}$. Additionally, we consider devices capable of generating a set of OPDs $\delta \in \{\delta_0, \dots, \delta_{L-1}\}$. The corresponding captured optical intensities $y(\delta_l)$ for $l \in \{0, \dots, L-1\}$ effectively sample the interferogram into L points.

We can then define the *transfer matrix* $\mathbf{A} \in \mathbb{R}^{L \times K}$, whose elements $a_{lk} = \mathbf{A}_{[l,k]} = A(\delta_l, \sigma_k)$ are obtained by sampling the response function. This transfer matrix \mathbf{A} defines the transformation from the discrete support of wavenumbers σ to that of OPDs δ , and each row of \mathbf{A} can be interpreted as an interferometer's response at a given OPD.

If the transfer matrix is used for system inversion, having fewer observations than unknowns (i.e., $L \leq K$) results in an *underdetermined* linear system. Conversely, if there are more observations than unknowns, the system is *overdetermined*.

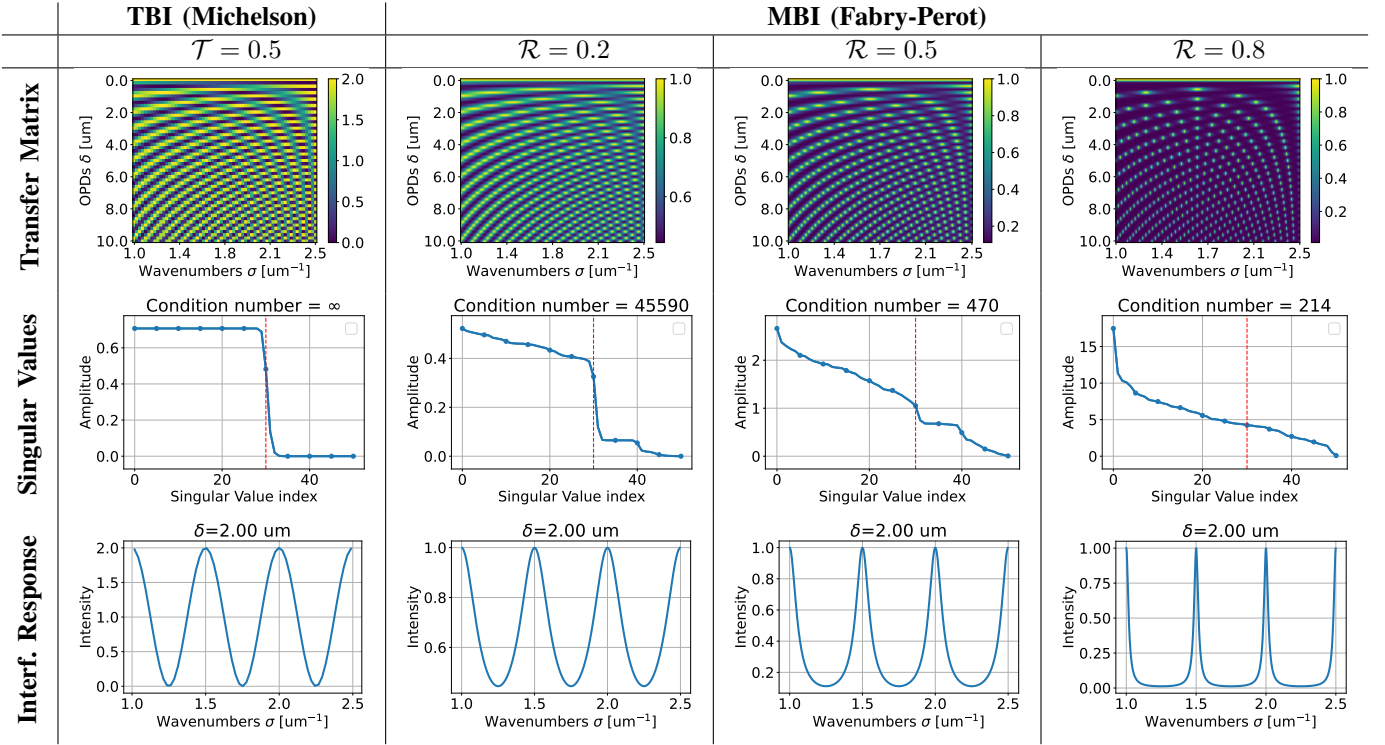


Fig. 3. Transfer matrices of some TBI (Michelson) and MBI (FP) instruments. Each row in the transfer matrices represents the interferometer response at a given OPD. The spectral support of the instruments is $\Omega \in [1, 2.5] \mu\text{m}^{-1}$, falling in the near-infrared and visible domains. The range of OPDs is arbitrarily chosen with $L = 51$ samples and a step of $\Delta\delta = 0.2 \mu\text{m}$, giving a Nyquist wavenumber $\sigma_{\text{Nyq}} = \sigma_{\text{max}}$. As such, Ω covers a ratio $\alpha = 0.6$ of the Nyquist range $[0, \sigma_{\text{Nyq}}]$. The wavenumbers in TBI are oversampled such that $K > L$ in order to observe the rankness and the sampling limit via the singular values, while those of MBI follow eq. (11).

In the analysis of the following sections, we assume that the coefficients of \mathbf{A} strictly follow the models described in eq. (2) and (4) for the TBI and MBI, respectively.

B. Sampling Analysis

For a proper representation of the response function $A(\delta, \sigma)$, it is necessary that the transfer matrix \mathbf{A} verifies the sampling theorem [35], [19]. This is required in order to properly represent the physical phenomena described by the continuous model. In particular, two conditions can be identified: one in the OPD domain and one in the wavenumber domain.

1) *OPD domain*: The OPD domain condition defines the main guidelines for the manufacturing of the device in order to accurately sample the observed interferogram $y(\delta)$. To this end we assume that the instrument samples in an OPD range $\delta \in \{0, \dots, \delta_{\text{max}}\}$ with a fixed step size $\Delta\delta$.

Using the sampling theorem, the maximum wavenumber representable by the discrete interferogram is $\sigma_{\text{Nyq}} = 1/(2\Delta\delta)$. Given the spectral support of the device $\Omega = [\sigma_{\text{min}}, \sigma_{\text{max}}]$, we need to impose $\sigma_{\text{Nyq}} \geq \sigma_{\text{max}}$, obtaining [19]:

$$\Delta\delta \leq \frac{1}{2\sigma_{\text{max}}}. \quad (10)$$

2) *Wavenumber domain*: The condition of the wavenumber domain is required to properly represent the oscillations of the filtering effect of the interferometer by sampling it without aliasing. In other words, \mathbf{A} must be able to represent the full spectral support from the responses shown in eq. (2) and (7)

in the TBI and MBI, respectively. This is equivalent to representing the highest cosine oscillation, yielding the following conditions for the sampling rate $\Delta\sigma$ of the wavenumbers [35]:

$$\Delta\sigma \leq \frac{1}{2(N-1)\delta_{\text{max}}}, \quad (11)$$

whereas in the TBI, as $N = 2$, this leads to $\Delta\sigma \leq 1/(2\delta_{\text{max}})$.

If eq. (11) is not verified, the transfer matrix \mathbf{A} does not properly represent the continuous system, as some of the interferometer responses are aliased.

C. Proposed formulation in terms of the DCT

Here, we formalize the conditions under which the physical models of the TBI and MBI can be expressed in terms of the DCT. Namely, the *Fourier cosine transforms* in eq. (3) and (8) become analogous to the DCT-II.

For that, considering the full Nyquist bandwidth $\Omega = [0, \sigma_{\text{Nyq}}]$, the OPDs and wavenumbers have to be regularly sampled into an equal number of samples $K = L$, with steps $\Delta\delta$ and $\Delta\sigma$, respectively, such that $\forall l, k \in \{0, \dots, K-1\}$:

$$\delta_l = l\Delta\delta, \quad \sigma_k = \left(k + \frac{1}{2}\right)\Delta\sigma, \quad \Delta\sigma\Delta\delta = \frac{1}{2K}, \quad (12)$$

Then, we can write the cosines in the models (2) and (4) as:

$$\cos[2\pi\delta_l\sigma_k] = \cos\left[\frac{\pi}{K}\left(k + \frac{1}{2}\right)l\right]. \quad (13)$$

The above equation shows that the DCT-II matrix representation is a special case of the transfer matrix of TBI, and that

of MBI without the harmonics, when the conditions in (12) are met.

Applying eq. (13) to (3) and (8), respectively, we obtain:

$$y_l = \frac{1}{2}y_0 + \text{DCT}_l(\mathbf{q} \odot \mathbf{x}), \quad (\text{TBI}), \quad (14a)$$

$$y_l = \langle \mathbf{q}, \mathbf{x} \rangle + 2 \sum_{n=1}^{N-1} \text{DCT}_l^{(n)}(\mathbf{q} \odot \mathbf{r}^n \odot \mathbf{x}), \quad (\text{MBI}), \quad (14b)$$

where we denote by $\mathbf{q} \in \mathbb{R}^K$ and $\mathbf{r} \in \mathbb{R}^K$ as the discretized versions of $\mathcal{Q}(\sigma)$ and $\mathcal{R}(\sigma)$ respectively, and by \odot and \oslash as the Hadamard (element-wise) product and division respectively. Additionally, $\text{DCT}_l(\cdot)$ denotes the l -th element of the DCT, while $\text{DCT}^{(n)}(\cdot)$ denotes the DCT carried out with the set of oscillations $\{n\delta_l\} \forall n \geq 2$, i.e., the harmonics. Note that imposing $K = L$ in eq. (14b) causes aliasing in the presence of non-negligible harmonics as it violates condition (11).

D. Spectral Resolution

In this section, we discuss some of the implications related to inverting the interferogram with approaches that are customarily employed in the TBI regime. Given the representation in terms of the DCT, it is often assumed to be a natural fit to apply approaches that operate in the Fourier domain, such as the one that will be discussed in Section IV-A. We carry out this analysis in terms of the spectral resolution of the reconstructed spectrum.

Having an OPD support within $[0, \delta_{\max}]$ is equivalent to windowing the interferogram signal by δ_{\max} . In the wavenumber domain, this is equivalent to a convolution by a cardinal sine function of width $1/(2\delta_{\max})$. Roughly, that is equal to the spectral resolution [19].

In MBI, applying the IDCT recovers not just the spectrum in $[\sigma_{\min}, \sigma_{\max}]$, but also some replicas placed at $[n\sigma_{\min}, n\sigma_{\max}]$, i.e. broadened by a factor of n , with $n \in \{2, \dots, N-1\}$. These replicas exhibit an exponential decay due to the harmonics. One could think of recovering the signal directly from those replicas, which enhances the spectral resolution roughly to $1/(2n\delta_{\max})$. While these broadened replicas provide finer detail, the robustness to noise is reduced because the replicas' intensities are attenuated by a factor of \mathcal{R}^n .

Regardless, this technique is often unfeasible, due to overlaps between these replicas. To avoid such overlaps, we must meet the condition:

$$\frac{\sigma_{\max} - \sigma_{\min}}{\sigma_{\min}} \leq \frac{1}{N-2}. \quad (15)$$

This is normally not a problem for TBI system, as this equation is automatically verified. Additionally, the situation worsens for larger $\Delta\delta$, as potential overlaps can arise through aliasing. Specifically, to represent all replicas without aliasing, we must be able to represent the spectrum up to a maximum wavelength $(N-1)\sigma_{\max}$. This imposes a stricter constraint than eq. (10), formulated as follows:

$$\Delta\delta \leq \frac{1}{2(N-1)\sigma_{\max}}. \quad (16)$$

In most practical scenarios, the above condition is overly restrictive for manufacturing real devices, especially multi-aperture ones. Therefore, performing such inversion for the

MBI with the same basic techniques that are applied for TBI instruments is often inefficient. It is instead preferable to conduct a more ad-hoc analysis, which we discuss in the following section.

Another manufacturing constraint is given by the need to increase of δ_{\max} to improve the spectral resolution. This requirement limits the miniaturizing capability of the instrument, particularly for multi-aperture devices [18].

E. Proposed System Analysis and Condition Number

When the spectrum reconstruction is obtained as a the least square solution, the approach involves a Moore-Penrose inversion of the transfer matrix, as detailed in Section IV-B. In this context, it is useful to characterize the inverse problem in terms of Hadamard, to verify if there is a need for regularization. We discuss this problem in terms of the condition number and of the matrix rank, both for the TBI and for the MBI. In the case of TBI, the system is often overdetermined and orthogonal, while in MBI, it is typically ill-conditioned, but could be overdetermined or underdetermined.

We denote by $R_{\mathbf{A}} \leq \min(L, K)$ the rank of \mathbf{A} and by $\{\psi_r\}_{r \in [1, \dots, R_{\mathbf{A}}]}$ the set of singular values in descending order. The condition number of \mathbf{A} is defined as [40]:

$$c = \psi_1/\psi_{R_{\mathbf{A}}} \geq 1, \quad (17)$$

where if $c = 1$, the singular values are equal and the problem is well-conditioned. If c is large or ∞ , the problem becomes ill-conditioned or ill-posed, respectively.

Fig. 3 visualizes different cases of transfer matrices of TBI and MBI models. We consider one case of TBI based on the Michelson model, as well as three cases of MBI based on the Fabry-Perot model with increasing reflectivity. In TBI the wavenumbers are oversampled (beyond the Nyquist limit), while in MBI the sampling rate follows eq. (11). In each case, we show the plots of singular values with the computed condition number. For the sake of demonstration, we plot an arbitrary interferometer responses (that is, a row of the matrix) at a given OPD. In the following, we use Fig. 3 as support to give some numeric examples, and we denote by $0 < \alpha \leq 1$ the portion that Ω occupies of the full Nyquist bandwidth $[0, \sigma_{\text{Nyq}}]$.

Here, we are not limited to the condition of no overlap of eq. (15), contrary to the case of IDCT. The signal can be fully recoverable as long as the continuous acquisition system is properly sampled and the condition number is low. To avoid aliasing we would however still require the sampling condition to hold (with the $N-1$ term), but we assume a more realistic case where $\sigma_{\max} < \sigma_{\text{Nyq}} < (N-1)\sigma_{\max}$. Specifically Fig. 3 shows $\sigma_{\text{Nyq}} = \sigma_{\max}$. Technically, this allows for the same spectral resolution of Section III-D but without the overlap condition, yet the condition number has to be verified.

1) *TBI*: The matrix is generated from fundamental cosine functions with equal magnitudes whose oscillations are equal to the OPDs, $\{\cos(2\pi\delta\sigma)\}$. If $\alpha = 1$ so that $\Omega = [0, \sigma_{\text{Nyq}}]$, we have an orthonormal basis. If Ω is sampled at the Nyquist limit following the conditions of Section III-C, \mathbf{A} becomes square and orthogonal. Then, $R_{\mathbf{A}} = K = L$ and $c = 1$.

In practical scenarios, where $\alpha < 1$ so that $\Omega \subset [0, \sigma_{\text{Nyq}}]$, we discuss that $R_{\mathbf{A}} \approx \alpha L$. For instance:

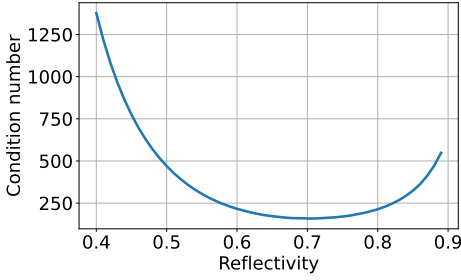


Fig. 4. The change of the condition number of the transfer matrix of a FPI with respect to reflectivity. The range of OPDs and wavenumbers is the same as that of Fig. 3. The condition number shows a minimum at $\mathcal{R} = 0.7$.

- If $\Delta\sigma = 1/(2\delta_{\max})$, i.e., at the Nyquist limit, we have $K \approx \alpha L$ samples in Ω (more rows than columns). Only the columns are linearly independent, which makes \mathbf{A} semi-orthogonal. The system is said to be overdetermined (more observations than unknowns), with $R_{\mathbf{A}} = K < L$. Here, the problem is well-posed since $c = 1$.
- If $\Delta\sigma < 1/(2\delta_{\max})$, i.e., oversampled, we have a linear dependency in both the columns and rows as Ω covers only a bandpass interval whose limit is at αL samples. \mathbf{A} is rank-deficient with $R_{\mathbf{A}} = \alpha L < \min(K, L)$. The singular values after the (αL) -th index drop to 0, leading to an ill-posed problem as $c \rightarrow \infty$.

To illustrate this more clearly, let us consider a numerical example, referring to the Michelson case of Fig. 3. In this example, we have $L = 51$, $\delta_{\max} = 10\mu\text{m}$, and $\Omega = [1, 2.5]\mu\text{m}^{-1}$ with $\alpha = 0.6$. The wavenumbers are oversampled such that $K > L$. The interferometer response shows a perfect cosine form. The singular values drop to 0 after the 31-st index, which means that \mathbf{A} is rank-deficient where $R_{\mathbf{A}} = 31 \approx \alpha L$ and $c \rightarrow \infty$. Therefore, for the TBI, assuming eq. (10), one can easily avoid the ill-posedness of the problem by properly choosing the sampling step $\Delta\sigma \geq 1/(2\delta_{\max})$, that is the minimum in terms of spectral resolution.

2) *MBI*: We assume here to be in the case in which either eq. (16) is not necessarily verified, or in other words some aliasing may appear due to the harmonics. In such case, the inversion of the matrix (e.g., the Moore-Penrose inverse) imposes the physical constraint that the OPDs are undersampled, causing the harmonics to mirror around $\sigma_{\text{Nyq}} = 1/(2\Delta\delta)$ and overlap.

To investigate this effect, coming from eq. (7), we can decompose the transfer matrix \mathbf{A} into the sum of components $\mathbf{A}^{(n)}$, each generated from weighted cosines of the n -th harmonic, as follows:

$$\mathbf{A}_{[l,k]} = \sum_{n=0}^{N-1} \mathbf{C}_{[k]}^{(n)} \cos\left[\frac{\pi}{K}nl\left(k + \frac{1}{2}\right)\right] = \sum_{n=0}^{N-1} \mathbf{A}_{[l,k]}^{(n)}, \quad (18)$$

where $\mathbf{C}_{[k]}^{(n)}$ is the discretized version of $C_n(\sigma)$ from eq. (6).

These harmonics (i.e., $n\delta_l \forall n \geq 2$) result in cosines at aliased OPD with exponentially smaller weights, which overlap with existing fundamental cosines.

If \mathcal{R} is very small, the overlaps involve very fast decaying cosines, which barely impact the recoverability in the range

of interest Ω . However, the harmonic coefficients that fall outside of that support are too much attenuated to allow for extra information to recovering the signal, making them indistinguishable to noise. If \mathcal{R} is very large, then the terms that fall outside the support Ω are more informative, while the information within Ω is mostly disrupted. Therefore, a balance has to be found. We can roughly investigate this effect by analyzing the singular values of \mathbf{A} . We analyze the condition number for $\alpha = 0.6$ in Fig. 3.

Let us compare the singular value decompositions (SVDs) of the MBI models. As the reflectivity increases, the steepness at the 31-st index is smoothed out as the matrix becomes full-rank. Furthermore, in Fig. 4, while we observe an improvement in the condition number as the reflectivity increases, it reaches a minimum at $\mathcal{R} = 0.7$ for the given set of OPDs.

The condition number shows that there is effectively a need for penalization or regularization even in the ideal textbook formalism. With real-world non-idealities like irregular sampling and variable reflectivity, this analysis becomes more complex. Nevertheless, the transfer matrix can still incorporate and represent this information. In the following section, we apply the same formalism but go beyond the textbook representation of the transfer matrix. We progressively introduce a more general formalism that is not limited to a specific form of the transfer matrix, gradually building towards the more comprehensive Bayesian framework.

IV. SPECTRUM RECONSTRUCTION

In this section, we describe a series of techniques for spectrum inversion, ending with our proposed solution. Specifically, the reconstruction problem is formalized as finding an estimation $\hat{\mathbf{x}} \in \mathbb{R}^K$ of an unknown spectrum $\mathbf{x} \in \mathbb{R}^K$ from the observed interferogram $\mathbf{y} \in \mathbb{R}^L$ given knowledge of the forward sensing model $\mathbf{A} \in \mathbb{R}^{L \times K}$. Generally speaking, \mathbf{A} is generated from the acquisition model of a given device following the framework of Section III. To streamline the exposition, these techniques are organized in an order that reflects their progression of applicability from more specific to more general scenarios. This increase in generality comes however with a decrease in computational speed.

In particular, we start with the IDCT in Section IV-A, the Moore-Penrose inverse in Section IV-B, the penalized inversion matrix in Section IV-C, concluding with the Bayesian formulation in Section IV-D. Finally, we specialize this framework for our proposed solution in Section IV-E.

A. Inversion from the Fourier Domain

Under the specific conditions outlined in Section III, where the transfer matrix \mathbf{A} strictly adheres to the model defined for the TBI or MBI, a straightforward reconstruction strategy for the spectrum entails an inversion from its expression given in the Fourier domain by the interferogram.

We begin by examining the TBI expression that we derived in eq. (14a). This equation shows that the sampled interferogram \mathbf{y} involves a DCT-II of the input spectrum. To invert this expression, a natural procedure involves employing the IDCT. As the DCT is nearly orthonormal, its inverse operation entails

a multiplication by a matrix whose coefficients mirror those of the DCT. The multiplication by this inverse matrix is formally known as DCT-III in the literature and denoted by $\text{IDCT}(\cdot)$ in the following.

Specifically, by manipulating eq. (14a), the spectrum can be reconstructed using the following procedure:

$$\begin{aligned} \text{IDCT}\left(\mathbf{y} - \frac{1}{2}y_0\right) &= \text{IDCT}\left(\text{DCT}(\mathbf{q} \odot \mathbf{x})\right) \\ \iff \hat{\mathbf{x}} &= \text{IDCT}\left(\mathbf{y} - \frac{1}{2}y_0\right) \odot \mathbf{q}. \end{aligned} \quad (19)$$

For the MBI, applying the same methodology presents certain challenges. In fact, performing a similar manipulation on eq. (14b) yields:

$$\begin{aligned} \text{IDCT}(\mathbf{y} - \langle \mathbf{q}, \mathbf{x} \rangle) &= \text{IDCT}\left(2\mathcal{Y}^{(1)} + 2\sum_{n=2}^{\infty} \mathcal{Y}^{(n)}\right) \\ &= 2\mathbf{q} \odot \mathbf{r} \odot \mathbf{x} + \boldsymbol{\xi}, \end{aligned} \quad (20)$$

where we have defined the harmonic terms $\mathcal{Y}^{(n)}$ and the corresponding ‘‘residuals’’ $\boldsymbol{\xi} \in \mathbb{R}^K$ from the inversion as:

$$\mathcal{Y}^{(n)} = \text{DCT}^{(n)}(\mathbf{q} \odot \mathbf{r}^n \odot \mathbf{x}), \quad (21a)$$

$$\boldsymbol{\xi} = \text{IDCT}\left(2\sum_{n=2}^{\infty} \mathcal{Y}^{(n)}\right). \quad (21b)$$

Essentially, the estimation of the spectrum would be accurate up to an unknown bias factor $\langle \mathbf{q}, \mathbf{x} \rangle$ on the interferogram \mathbf{y} , if not for the presence of the residuals $\boldsymbol{\xi}$. This analysis mirrors that of Section III-D, with the residuals $\boldsymbol{\xi}$ representing the replicas due to harmonics; as such, the sampling theorem imposes that eq. (16) must be met to avoid aliasing.

In [34], an analytical method for spectrum reconstruction has been proposed in order to compensate the harmonic overlap. This method uses a Haar function to expand the DFT of the interferogram and the unknown spectrum. However, the applicability of this method is still limited by reflectivity and transmittance of the acquisition system, which is assumed constant over the spectral range. Moreover, its spectral resolution is limited by the Nyquist bandwidth since it is based on the DFT of the interferogram.

B. Moore-Penrose inversion (Pseudo-inversion)

In practical scenario, the device can be characterized with a controlled measurement [8]. This procedure can be employed to obtain coefficients of the transfer matrix \mathbf{A} which allow for a more realistic representation of the system with respect to the theoretical models described in Section II. This includes some non-idealities that affect most real world acquisition systems (e.g., irregular sampling, variable reflectivity, harmonic contribution, measurement noise). This necessity demands for more general approaches for inversion that can be applied to transfer matrices \mathbf{A} of any sort.

The most naive approach in this direction is to estimate the spectrum through an inversion of \mathbf{A} , or more specifically a Moore-Penrose inversion (also known as the pseudo-inversion), as the matrix is not necessarily square, nor full rank. In other words, the estimation is given by:

$$\hat{\mathbf{x}} = \mathbf{A}^\dagger \mathbf{y}, \quad (22)$$

where $\mathbf{A}^\dagger \in \mathbb{R}^{L \times K}$ denotes the pseudo-inverse of \mathbf{A} . As the non-zero singular values of \mathbf{A}^\dagger are the reciprocal of those of \mathbf{A} , the two matrices exhibit the same condition number. In this case, the analysis of Section III-E holds, and the approach is applicable when \mathbf{A} has a small enough condition number.

In particular, the IDCT procedure, analyzed in the previous section for the ideal TBI expression, is a special case of the pseudo-inversion that operates under well-behaved conditions.

C. Inversion with Penalized Singular Values

To overcome the limitations of the pseudo-inversion approach, a series of methods were developed in the literature to directly adjust the condition number of \mathbf{A}^\dagger , introducing some penalization on its singular values [40]. For such methods, let us impose that the estimation $\hat{\mathbf{x}} = \tilde{\mathbf{A}}\mathbf{y}$ is carried out with a modified version $\tilde{\mathbf{A}}$ of \mathbf{A}^\dagger .

Given $r \in \{1, \dots, R_{\mathbf{A}}\}$, let us define ψ_r and $\tilde{\psi}_r$ as the singular values of \mathbf{A} and $\tilde{\mathbf{A}}$, respectively. Two of the most widespread techniques for singular value penalization are:

1) *Truncated singular value decomposition (TSVD)*: [43], where a given percentage $0 < \lambda < 1$ of the singular values of \mathbf{A}^\dagger is kept unmodified and the rest are set to zero, i.e.:

$$\tilde{\psi}_r = \begin{cases} 1/\psi_r, & \text{if } r < \lambda R_{\mathbf{A}}. \\ 0, & \text{otherwise.} \end{cases} \quad (23)$$

2) *Ridge regression (RR)*: [44], where the singular values are dampened by a penalization parameter $\lambda > 0$:

$$\tilde{\psi}_r = \frac{\psi_r}{\psi_r^2 + \lambda^2}, \quad (24)$$

which can be easily be shown that it is equivalent to the closed-form solution of the following minimization problem:

$$\hat{\mathbf{x}} = \underset{\mathbf{x}}{\text{argmin}} \frac{1}{2} \|\mathbf{y} - \mathbf{A}\mathbf{x}\|_2^2 + \lambda^2 \|\mathbf{x}\|_2^2. \quad (25)$$

D. Bayesian Inversion

In the Bayesian framework, the optical acquisition phenomenon is modeled as:

$$\mathbf{y} = \mathbf{A}\mathbf{x} + \mathbf{e}, \quad (26)$$

where the observed interferogram \mathbf{y} is expressed as the sum of a deterministic component $\mathbf{A}\mathbf{x}$ and a stochastic additive noise $\mathbf{e} \in \mathbb{R}^L$.

In the case \mathbf{e} is assumed to be Gaussian, the maximum a posteriori estimator $\hat{\mathbf{x}}$ of the latent variable \mathbf{x} can be written in the form [45] :

$$\begin{aligned} \hat{\mathbf{x}} &= \underset{\mathbf{x}}{\text{argmin}} h(\mathbf{x}) + \lambda g(\mathbf{L}\mathbf{x}) \\ &= \underset{\mathbf{x}}{\text{argmin}} \frac{1}{2} \|\mathbf{A}\mathbf{x} - \mathbf{y}\|_2^2 + \lambda g(\mathbf{L}\mathbf{x}), \end{aligned} \quad (27)$$

where $h(\mathbf{x}) = \frac{1}{2} \|\mathbf{A}\mathbf{x} - \mathbf{y}\|_2^2$ is the data fidelity term, $g(\cdot)$ denotes a scalar functional, \mathbf{L} is a generic linear operator, and λ is a regularizing parameter. One can easily verify that the pseudo-inversion method is a special case, providing the closed form solution given in eq. (22) for the above minimization problem when $\lambda = 0$.

Moreover, eq. (25) for ridge regression is a particular application of the Bayesian framework with the function $g(\cdot)$ expressed as the squared ℓ_2 norm and \mathbf{L} set as the identity operator. Effectively, the introduction of the regularization function $g(\mathbf{L}\mathbf{x})$ can be seen as a way to impose the well-posedness to the solution, similarly to how it was done for the regularized singular values. In the framework of Bayesian inference, this can be interpreted as the prior information on the spectra that are expected to be captured by the device.

When obtaining a closed-form solution is not feasible, e.g. when $g(\cdot)$ is not differentiable, *iterative algorithms* become prominent for solving eq. (27). Approaches such as those based on proximal splitting [46] are commonly employed in such cases. These methods begin with an initial guess, iteratively update the inferred solution in successive steps, and continue this process until convergence is reached.

E. Proposed Reconstruction Solution

In this section, we propose to specify the Bayesian framework with sparsity-inducing priors [36]. This approach, known as LASSO [47], assumes that the cost function from eq. (27) is rewritten as:

$$\hat{\mathbf{x}} = \underset{\mathbf{x}}{\operatorname{argmin}} \frac{1}{2} \|\mathbf{A}\mathbf{x} - \mathbf{y}\|_2^2 + \lambda \|\mathbf{L}\mathbf{x}\|_1, \quad (28)$$

where $\|\cdot\|_1$ denotes the ℓ_1 -norm.

In these approaches, \mathbf{L} is chosen to define a transformation to a sparse domain. We specifically consider two scenarios:

1) *Sparsity on the Fourier domain of the spectrum*: We wish to impose a sparsity-inducing regularizer on the Fourier domain of the spectrum, i.e., the DCT in this case, where low-amplitude high frequency oscillations can be softly discarded. Said oscillations may occur due to noisy components in nature. For that, we define $\mathbf{L} \in \mathbb{R}^{K \times K}$ as the orthogonal version of the Type-II DCT, whose elements are:

$$l_{ij} = \sqrt{\frac{2}{J}} \cos \left[\frac{\pi}{J} \left(j + \frac{1}{2} \right) i \right]_{\forall i, j \in \{0, \dots, K-1\}}, \quad (29)$$

with l_{0j} divided by $\sqrt{2} \forall j$. This transformation allows to express the spectrum in a complementary Fourier domain and is related to the space of the interferogram.

2) *Sparsity on the spectrum itself*: In the case of interferograms acquired from light with monochromatic or specific wavenumbers, we know already that the spectra that we wish to reconstruct are sparse. We wish to impose sparsity on the spectrum itself, with LASSO acting as feature selection of the wavenumbers of interest. Accordingly, we define \mathbf{L} as the identity operator \mathbf{I}_K , resulting in the following cost function:

$$\hat{\mathbf{x}} = \underset{\mathbf{x}}{\operatorname{argmin}} \frac{1}{2} \|\mathbf{y} - \mathbf{A}\mathbf{x}\|_2^2 + \lambda \|\mathbf{x}\|_1. \quad (30)$$

We propose to employ the Loris-Verhoeven (LV) optimizer [45] for the solution of eq. (28). The LV optimizer is an iterative algorithm applicable to any inversion problem with a quadratic data term and a non-differentiable convex function $g(\cdot)$. As this solver does not require any matrix inversion and provides easy-to-follow guidelines to set the convergence

Algorithm 1 Proposed method using the LV algorithm [45]

Require: \mathbf{A} , \mathbf{L} , N_{iters}
Initialize $\mathbf{x}^{(0)} = \mathbf{A}^T \mathbf{y}$, $\mathbf{u}^{(0)} = \mathbf{L}\mathbf{x}^{(0)}$
Initialize $\tau = 0.99 / \|\mathbf{A}\|_{\text{op}}^2$, $\eta = 1 / (\tau \|\mathbf{L}\|_{\text{op}}^2)$, and $\rho = 1.9$
Define $\operatorname{prox}_{\lambda, g^*}(\mathbf{u}) = \min(\max(\mathbf{u}, -\lambda), \lambda)$
for $q = 0$ to $N_{\text{iters}} - 1$ **do**
 $\mathbf{e}^{(q)} = \mathbf{A}^T (\mathbf{A}\mathbf{x}^{(q)} - \mathbf{y})$
 $\mathbf{x}^{(q+\frac{1}{2})} = \mathbf{x}^{(q)} - \tau (\mathbf{e}^{(q)} + \mathbf{L}^T \mathbf{u}^{(q)})$
 $\mathbf{u}^{(q+\frac{1}{2})} = \operatorname{prox}_{\lambda, g^*} \left(\mathbf{u}^{(q)} + \eta \mathbf{L}\mathbf{x}^{(q+\frac{1}{2})} \right)$
 $\mathbf{x}^{(q+1)} = \mathbf{x}^{(q)} - \rho \tau (\mathbf{e}^{(q)} + \mathbf{L}^T \mathbf{u}^{(q+\frac{1}{2})})$
 $\mathbf{u}^{(q+1)} = \mathbf{u}^{(q)} + \rho (\mathbf{u}^{(q+\frac{1}{2})} - \mathbf{u}^{(q)})$
end for
return $\hat{\mathbf{x}} = \mathbf{x}^{(N_{\text{iters}})}$

parameters, it is more suitable for our problem than its competitors [48]. In particular, eq. (30) is traditionally solved with algorithms based on iterative shrinkage-thresholding algorithm (ISTA), such as FISTA [49], however, the proposed solver is able to generalize to both sparsity scenarios that we consider in our work.

Algorithm 1 describes the iterative updates of LV for the estimation of \mathbf{x} and of the dual parameter \mathbf{u} . $\|\mathbf{A}\|_{\text{op}}$ and $\|\mathbf{L}\|_{\text{op}}$ represent the operator norms of \mathbf{A} and \mathbf{L} respectively [48]. η and τ are convergence parameters such that $\eta\tau \leq 1 / \|\mathbf{L}\|_{\text{op}}^2$, and $1 \leq \rho \leq 2$ is the over-relaxation parameter; their specified values were chosen according to the relevant literature [48].

In the third step of the update, $\operatorname{prox}_{\lambda, g^*}(\mathbf{u})$ denotes the proximal operator associated to the Fenchel conjugate of $g(\cdot)$ [50]. This is equal to a hard-thresholding operator when g is chosen as the ℓ_1 norm. That is:

$$\operatorname{prox}_{\lambda, g^*}(\mathbf{u}) = \min(\max(\mathbf{u}, -\lambda), \lambda), \quad (31)$$

where $\min(\cdot, \cdot)$ and $\max(\cdot, \cdot)$ respectively denote the minimum and maximum operator, applied on every element of the first argument.

V. EXPERIMENTS ON SIMULATED DATA

In this section, we aim to show the limitations of the spectrum reconstruction algorithms in terms of applicability to various case studies. To this end we go through the methods following the order described in Section IV and showing that the reconstruction results become less and less accurate the further we move from a baseline case, while taking the chance to discuss on the robustness of the methods.

In particular, we simulate three acquisition scenarios of non-idealities from the textbook models: reflectivity regimes (Section V-C), irregular sampling of the OPDs (Section V-D), and noise corruption (V-E).

A. Dataset Description

The simulated datasets include two collection of spectra, labeled Solar and Specim. In particular, Solar contains $M = 22$ solar spectra acquired at different times of the day. Its spectral support is $\Omega = [1.000, 2.850] \mu\text{m}^{-1}$. Specim contains the spectra of the central pixel of each of the $M = 24$ color boxes

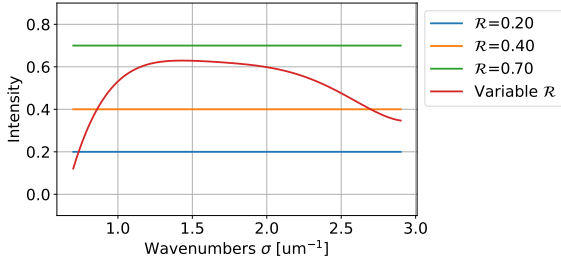


Fig. 5. Different reflectivity regimes.

of a Classic ColorChecker, acquired with the *Specim IQ* hyperspectral camera. Its spectral support is $\Omega = [0.996, 2.517] \mu\text{m}^{-1}$. When simulating interferograms from such spectra, we consider $L = 319$ OPD samples, to match the specifications of the interferometric spectrometer Imaging SPectrometer On Chip (ImSPOC) UV 2. The simulation is carried out using the transfer matrix obtained by sampling eq. (4) for the MBI and applying the model of eq. (26) to simulate the interferogram.

Unless otherwise stated, no noise is added, and the OPD support is regularly sampled with a step size $\Delta\delta = 0.175 \mu\text{m}$, i.e., $\delta \in [0, 55.65] \mu\text{m}$. We also set a reflectivity $\mathcal{R} = 0.2$ and transmissivity $\mathcal{T} = 1$.

B. Experimental Setup

We perform a qualitative analysis of the reconstruction by varying the parameters from the baseline acquisition model described in the previous section. We compare the IDCT method from eq. (19), Haar method [34], and the pseudo-inverse (PINV) of eq. (22). When noise is present, we also compare with truncated singular value decomposition (TSVD) [44] and ridge regression (RR) [43] that we detailed in Section IV-C, as well as our proposed method. Those were ignored in the noiseless case, as the optimal parametric choice makes them equivalent to the pseudo-inversion.

In terms of notation, we denote by $\mathbf{Y} \in \mathbb{R}^{L \times M}$ the set of observed interferograms, by $\mathbf{X} \in \mathbb{R}^{K \times M}$ the reference spectra, and by $\hat{\mathbf{X}} \in \mathbb{R}^{K \times M}$ the corresponding reconstructed spectra.

The results are assessed quantitatively using the root mean squared error (RMSE) quality index:

$$\text{RMSE} = \frac{\|\mathbf{X} - \hat{\mathbf{X}}\|_F^2}{\|\mathbf{X}\|_F^2}. \quad (32)$$

C. Reflectivity

In this section we assume that the transfer matrix \mathbf{A} follows the MBI formulation with constant reflectivity values in the set $\mathcal{R} = \{0.2, 0.4, 0.7\}$, as well as a case where the reflectivity varies with respect to σ , extracted from the characterization of a real device [8]. Fig. 5 shows these reflectivity regimes. The Haar method is not applicable to the case of varying reflectivity, but we still apply it assuming that the reflectivity is equal to its mean value over the spectral range of reconstruction.

Fig. 6 shows the results of inverting simulated Solar and Specim interferograms in each case. As expected, the IDCT performs better for low values of reflectivity, as the model is

TABLE I
RESULTS OF THE SIMULATED EXPERIMENTS SHOWING THE RMSE AND THE OPTIMAL REGULARIZING PARAMETER λ_{opt} .

Dataset	Method	SNR = 20 dB		SNR = 15 dB	
		λ_{opt}	RMSE	λ_{opt}	RMSE
Solar	IDCT	-	0.087	-	0.145
	Haar [34]	-	0.099	-	0.161
	TSVD [43]	0.648	0.110	0.648	0.186
	RR [44]	7.565	0.113	10.723	0.186
	Ours	16.768	0.071	29.471	0.079
Specim	IDCT	-	0.142	-	0.180
	Haar [34]	-	0.112	-	0.160
	TSVD [43]	0.539	0.098	0.533	0.166
	RR [44]	6.136	0.102	7.055	0.173
	Ours	7.197	0.084	12.649	0.109

more similar to the TBI, as especially evident for the Specim case. The Haar method is more robust to the increase of reflectivity, but the reconstruction results tend to fail for high reflectivity regimes, possibly since such regimes are susceptible to aliasing, and are inaccurate for varying reflectivity. The pseudo-inversion generates basically perfect matches, as the noiseless case requires no regularization and we exploit the perfect knowledge of the system through \mathbf{A} .

D. Irregular Sampling

Compared to the baseline setup, in this experiment we simulate the interferograms assuming that the OPD domain is irregularly sampled, or in other words that $\Delta\delta$ is not constant. In particular, we use the OPD values that were characterized in the study of [8], whose mean and standard deviation on $\Delta\delta$ are 0.17 and 0.15 μm , respectively.

Fig. 7 shows the results of inverting simulated Solar and Specim interferograms. As expected, the Fourier-based approaches, IDCT and Haar, exhibit many mismatches as they require the OPD support to be regularly sampled. The pseudo-inverse however shows perfect matches as this non-ideality is already embedded in the matrix \mathbf{A} .

E. Noise Corruption

In this experiment we aim to show the robustness of the proposed algorithm when the interferograms are corrupted by noise. In particular, we corrupt the simulated interferograms by adding Gaussian noise with SNR of 20 and 15 dB.

For each method, the optimal regularization parameter λ_{opt} is chosen with a grid search to minimize the RMSE. TABLE I shows a summary of the results. Fig. 8 shows a selected spectrum from each of the Solar and Specim datasets. The proposed method based on LV outperforms the other approaches in terms of RMSE, which are greatly affected by the noise. We also give some insights on the regularizing parameter and robustness to noise.

In TABLE I, first, the IDCT and the Haar methods fail to attenuate the noise. Second, as the SNR decreases, the values of λ_{opt} in RR and our proposed method increase.

In fact, for low SNRs, the higher-order harmonics get confused with the noise energy. This limits the resolving power of the data term in the cost function, demanding for a larger

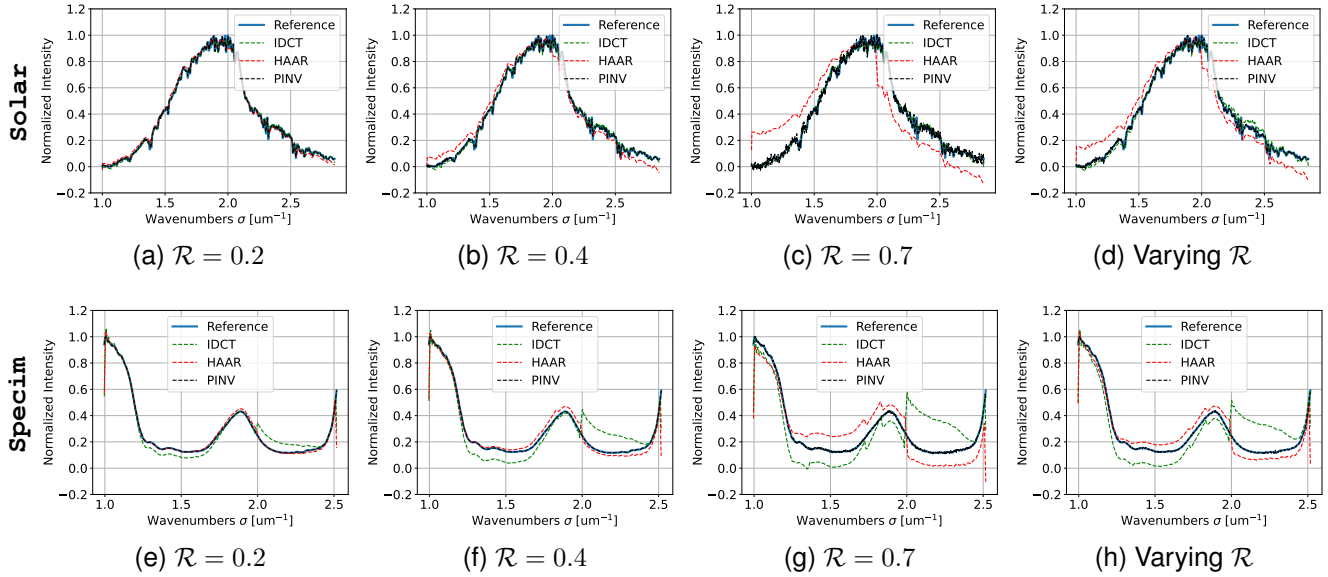


Fig. 6. Reconstruction of spectra with different values of reflectivity. The two rows refer respectively to the Solar and Specim datasets.

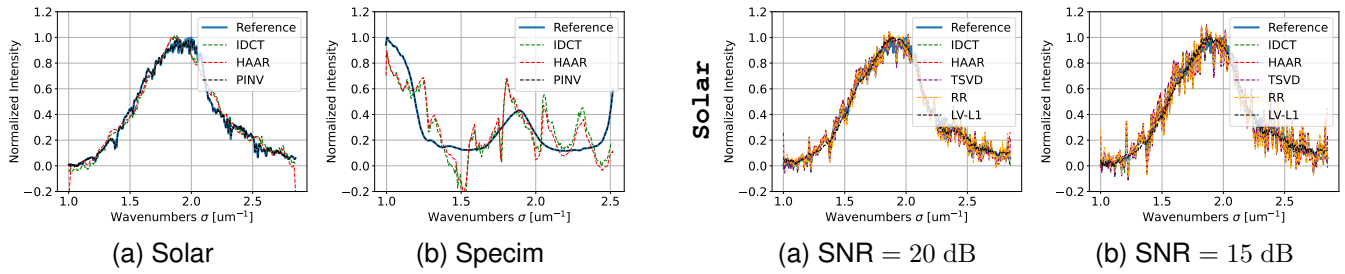


Fig. 7. Reconstruction with irregular OPD sampling.

penalization factor. On the other hand, the values of λ_{opt} in the case of TSVD remain unchanged.

Fig. 8 confirms this analysis. The reconstruction based on induced sparsity fits better with the reference, noting that some high oscillation components are lost in low SNR regimes [19]. For the other approaches, even if the reconstruction loosely follows the shape of the references, the spectra remain noisy.

VI. EXPERIMENTS ON REAL DATA

In this section, we perform spectral reconstructions for real interferograms measured using a multi-aperture FP-based device, comparing the accuracy the results among the methods that were discussed in Section IV. In particular we aim to reconstruct monochromatic sources with the same optical energy and verify if the inferred reconstruction stays flat across the wavenumber range.

A. Dataset Description

The real datasets include two collections of interferograms, labeled MC-451 and MC-651, whose characteristics are summarized in TABLE II. These interferograms were measured using the ImSPOC UV 2 device, shown in Fig.9a. This instrument is composed of an array of 319 Fabry-Perot etalons

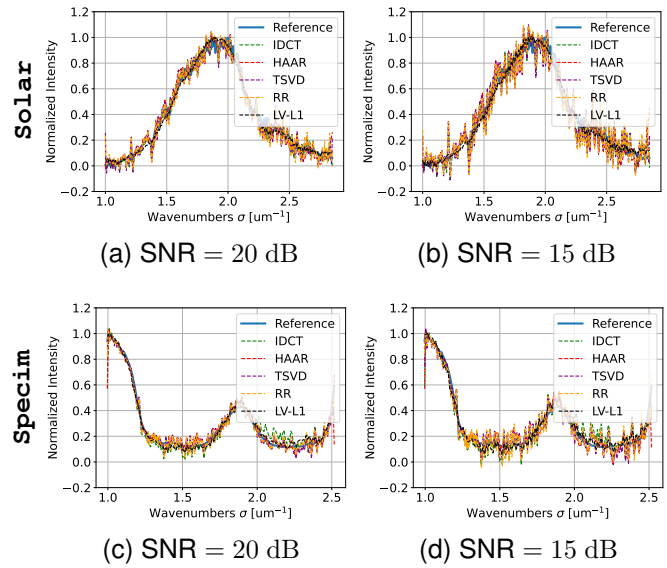


Fig. 8. Reconstruction of spectra from interferograms with noise corruption. The two rows refer respectively to the Solar and Specim datasets.

TABLE II
CHARACTERISTICS OF THE REAL INTERFEROMETRIC DATASETS CAPTURED WITH IMSPQC UV 2 [18]. THE RANGE OF CENTRAL WAVENUMBERS AND THAT OF OPDs [8] ARE REPORTED.

Dataset	No. of acq.s, M	No. of OPDs, L	OPD range δ (μm)	Central wn. range (μm^{-1})
MC-451	451	319	[1.79, 55.87]	[1.00, 2.85]
MC-651	651	319	[1.75, 55.78]	[1.10, 2.85]

with nominal increasing thickness of step size $\Delta d = 87.5$ nm, shown in Fig.9b.

The acquisitions were performed in a controlled environment, with the input spectra being obtained by modulating a known light source through a tunable diffraction grating, using

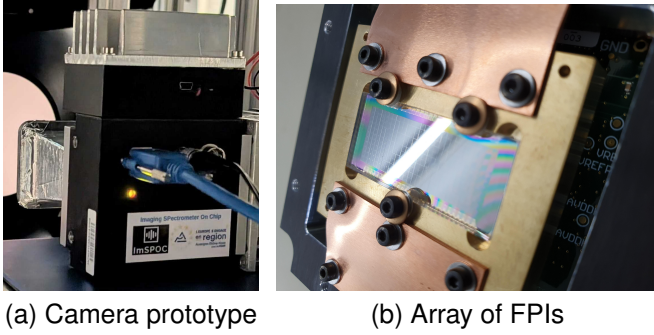


Fig. 9. Left: The ImSPOC prototype used to acquire the real datasets. Right: The array of 11×29 Fabry-Perots etalons that composes the prototype.

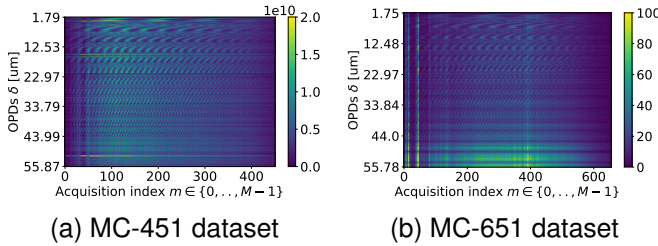


Fig. 10. Visualization of the real datasets. Each column represents an interferogram acquired from a monochromatic source.

the setup described in [8]. Given the monochromatic nature of the inputs, we assume in this study that the columns of the reference spectra $\mathbf{X} \in \mathbb{R}^{K \times M}$ are Dirac pulses centered at the nominal central wavenumber of the diffraction grating. In particular, we have $M = 451$ and $M = 651$ central wavenumbers for the MC-451 and the MC-651 datasets, respectively.

B. Experimental Setup

For the reconstruction, we assume that the transfer matrix \mathbf{A} is once again obtained as a sampled version of eq. (4) for the MBI. However, compared to the previous set of experiments, we use here a 5-th order polynomial function to express the dependency of $\mathcal{R}(\sigma)$ and $\mathcal{T}(\sigma)$ on the wavenumbers σ . Moreover, the OPD support is not regularly sampled and starts from $\delta_{min} \approx 1.75$, missing around 10 samples in average. In the experiments, the OPD support is extrapolated from $\delta = 0$, and the transfer matrix can then be generated for any range of values of wavenumbers and OPDs.

The expression of reflectivity, transmissivity, and OPD that we plug in the transfer matrix \mathbf{A} follows the characterization of the instrument performed by the second author in [8]. The characterization makes use only of the MC-451 dataset.

On the other hand, the interferograms of MC-651, which were acquired at a different time, were never used in the calibration process. This makes the MC-651 dataset particularly valuable for testing, as it provides an independent set of data that was not seen during training (i.e., calibration).

Fig. 11 shows the coefficients of \mathbf{A} and its singular values. The condition number is high, showing that the problem is ill-conditioned and cannot be solved without some sort of regularization. Consequently, compared to the previous

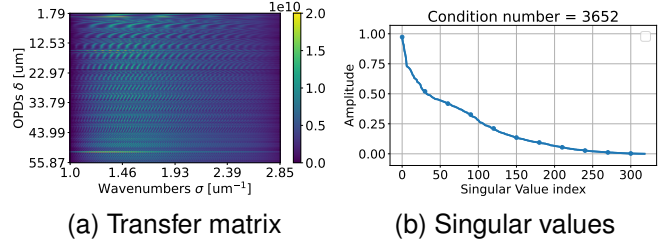


Fig. 11. Transfer matrix \mathbf{A} , parametrized from the dataset MC-451.

TABLE III
RESULTS OF THE REAL EXPERIMENTS SHOWING THE RMSES AND THE NUMBER OF MCW. THE BEST RESULTS ARE MARKED IN **BOLD**.

ImSPOC UV 2: Array of Fabry-Perot ∞ -wave model					
Dataset	Method	λ_{opt}	Diagonal RMSE	Full RMSE	No. of MCW
MC-451	TSVD [43]	0.600	0.499	0.963	408
	RR [44]	0.316	0.472	0.937	423
	Ours (1k iters.)	0.215	0.388	0.800	403
	Ours (50k iters.)	0.054	0.221	0.463	429
MC-651	TSVD [43]	0.320	0.784	1.244	444
	RR [44]	2.512	0.781	1.242	429
	Ours (1k iters.)	1.000	0.547	0.959	426
	Ours (50k iters.)	0.341	0.542	0.879	<u>440</u>

testbed, we do not provide results for the pseudo-inverse method. We also exclude the IDCT and Haar methods, as they are not applicable to this scenario. For our proposed method, we impose sparsity in the spectral domain, following eq. (30).

First, we assess the results based on the RMSE metric, with the identity matrix \mathbf{I}_K as reference. Second, we introduce the *number of matching central wavenumbers (MCW)* as a quality metric; this metric defines the number of times the maxima of the reconstructed spectra match with the nominal central wavenumbers of the corresponding interferograms. For instance, denoting by $\hat{\mathbf{x}}_m$ the m -th column of $\hat{\mathbf{X}}$ and $\hat{k} = \text{argmax}_k(\hat{\mathbf{x}}_m)$:

$$\text{MCW}(\hat{\mathbf{X}}) = \sum_{m=0}^{M-1} \mathbb{1}_{\{m, \hat{k}\}} \text{ with } \mathbb{1}_{\{m, k\}} = \begin{cases} 1, & \text{if } k = m. \\ 0, & \text{otherwise.} \end{cases} \quad (33)$$

For each method, we explored the range of regularization parameters with a grid search within reasonable intervals.

C. Reconstruction Results

TABLE III shows a summary of the results. Overall, the proposed solution outperforms the other techniques in terms of RMSE, even at a lower number of iterations, and is at least competitive in terms of the number of MCW with respect to TSVD and RR.

Fig. 12 plots the maxima of the reconstructed spectra with respect to the associated nominal central wavenumbers, for the two datasets. Moreover, the points in the plots are color-coded in orange if the maximum value of the reconstructed spectra matches with the central wavenumber of the reference. Compared to conventional techniques, our algorithm produces a plot of the maxima of the reconstructed spectra that is overall flatter. This is more evident for the MC-451, as the transfer matrix \mathbf{A} closely matches the acquisition conditions. However, decent results are also obtained for MC-651 dataset.

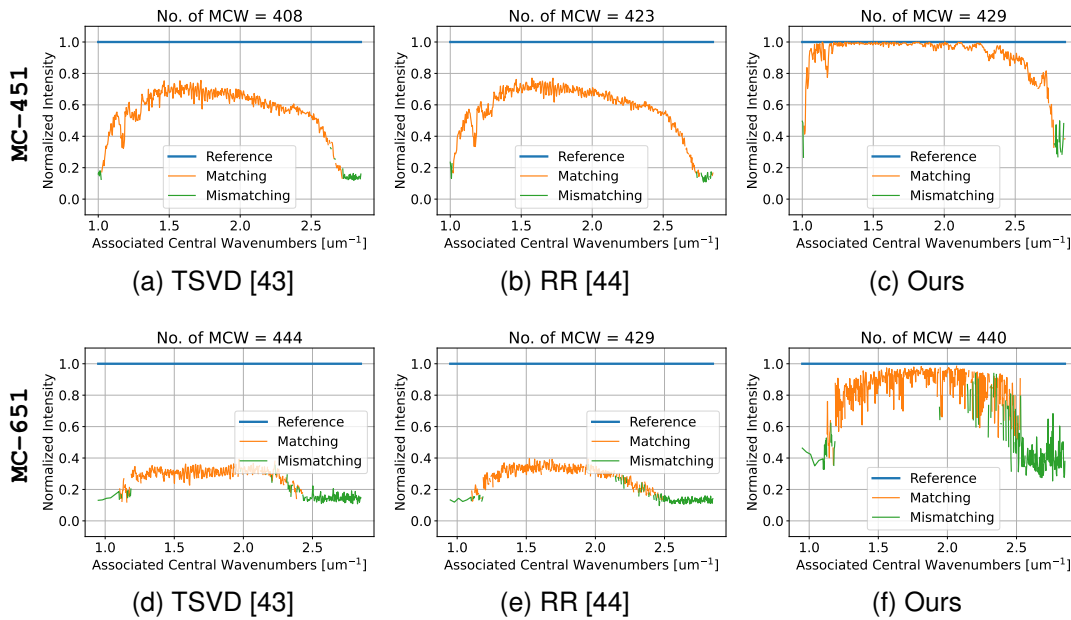


Fig. 12. Visualization of the maximum of the reconstructed spectra in $\hat{\mathbf{X}}$, classified into those that match with the corresponding nominal central wavenumbers. The two rows refer to the MC-451 and MC-651 datasets, respectively.

VII. CONCLUSION

In this work, we tackle the problem of MBI spectroscopy, as we propose a generalized unified framework for the analysis and the spectrum reconstruction in both TBI and MBI. At its core, the framework relies on the representation of the continuous physical models by the discretized transfer matrix. First, we perform a numerical analysis on the transfer matrices in TBI and MBI under the textbook formulation and formalize their limitations in terms of spectral resolution and the condition number. Second, we extend the range of spectrum reconstruction techniques while trying to tackle real-world acquisition non idealities, as we showcase an increasingly generic framework based on the Bayesian inversion. The findings are validated on simulated interferograms by considering one non ideality at a time (reflectivity levels, irregular sampling, and noise measurements), and on real interferograms acquired from monochromatic spectral sources. In the future, we plan to expand the reconstruction to hyperspectral cubes by taking into account spatial information, and extend our database with more acquisitions for deep learning approaches.

ACKNOWLEDGMENTS

We thank Dr. Bernard Shmidt for assistance with acquiring the SHINE and SPECIM datasets, and Dr. Silvère Gousset for help with the MC-451 and MC-651 datasets.

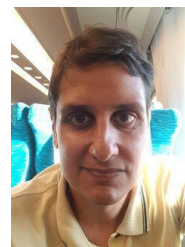
REFERENCES

- [1] M. T. Eismann, *Hyperspectral remote sensing*, ser. Press Monographs. Society of Photo-Optical Instrumentation Engineers, 2012.
- [2] D. Manolakis, R. Lockwood, and T. Cooley, *Hyperspectral imaging remote sensing: Physics, sensors, and algorithms*. Cambridge University Press, 2016.
- [3] C. Zhu, H. Zheng, Y. Yuan, and L. Su, "Spectrum reconstruction of multispectral light field imager based on adaptive sparse representation," *IEEE Transactions on Instrumentation and Measurement*, 2023.
- [4] T. Pan, C. Wu, and Q. Chen, "Sparse reconstruction using block sparse bayesian learning with fast marginalized likelihood maximization for near-infrared spectroscopy," *IEEE Transactions on Instrumentation and Measurement*, vol. 71, pp. 1–10, 2021.
- [5] M. Born and E. Wolf, *Principles of optics: Electromagnetic theory of propagation, interference and diffraction of light*. Elsevier, 2013.
- [6] P. Hariharan, *Basics of interferometry*. Elsevier, 2010.
- [7] E. Hecht, *Optics (5th edition)*. Pearson, 2016.
- [8] D. Picone, S. Gousset, M. Dalla Mura, Y. Ferrec, and E. le Coarer, "Interferometer response characterization algorithm for multi-aperture Fabry-Perot imaging spectrometers," *Optics Express*, vol. 31, no. 14, pp. 23 066–23 085, 2023.
- [9] C. Zhu, Y. Zhuang, B. Liu, and J. Huang, "Review of fiber optic displacement sensors," *IEEE Transactions on Instrumentation and Measurement*, vol. 71, pp. 1–12, 2022.
- [10] J. Bläsi, R. De La Rue, and M. Gerken, "Pattern design of diffractive optical sensor elements for multiplex interferometry," *IEEE Transactions on Instrumentation and Measurement*, 2023.
- [11] B. Fang, S. Zhong, Q. Zhang, J. Zhong, Q. Lin, Y. Yu, and Z. Peng, "Full-range line-field optical coherence tomography for high-accuracy measurements of optical lens," *IEEE Transactions on Instrumentation and Measurement*, vol. 69, no. 9, pp. 7180–7190, 2020.
- [12] J. Gao, B. Deng, Y. Qin, X. Li, and H. Wang, "Point cloud and 3-d surface reconstruction using cylindrical millimeter-wave holography," *IEEE Transactions on Instrumentation and Measurement*, vol. 68, no. 12, pp. 4765–4778, 2019.
- [13] C. M. Holler, M. E. Jones, A. C. Taylor, A. I. Harris, and S. A. Maas, "A 2–20-ghz analog lag correlator for radio interferometry," *IEEE Transactions on Instrumentation and Measurement*, vol. 61, no. 8, pp. 2253–2261, 2012.
- [14] U. A. Khan, N. Nguyen, and M. N. Afsar, "Millimeter-and submillimeter-wave dielectric measurements of household powders using fourier transform spectroscopy," *IEEE Transactions on Instrumentation and Measurement*, vol. 57, no. 2, pp. 286–293, 2008.
- [15] H. Zhang, L. Xu, Y. Pang, and Z. Cao, "Gas temperature measurement by aligning absorption spectroscopy of dual-phase-unlocked optical combs," *IEEE Transactions on Instrumentation and Measurement*, vol. 71, pp. 1–10, 2022.
- [16] A. P. Hungund, H. Tekle, B. Zhang, R. J. O'Malley, J. D. Smith, R. E. Gerald, and J. Huang, "Real-time air gap and thickness measurement of continuous caster mold flux by extrinsic fabry-perot interferometer," *IEEE Transactions on Instrumentation and Measurement*, 2023.
- [17] P. Fellgett, "The nature and origin of multiplex Fourier spectrometry," *Notes and Records of the Royal Society*, vol. 60, no. 1, pp. 91–93, 2006.

- [18] N. Guerineau, E. Le Coarer, Y. Ferrec, and F. De La Barriere, "Fourier transform multi-channel spectral imager," Jan. 2018, FR patent 1.656.162.
- [19] W. B. Cook, H. E. Snell, and P. B. Hays, "Multiplex Fabry-Perot interferometer: I. Theory," *Applied Optics*, vol. 34, no. 24, pp. 5263–5267, 1995.
- [20] D. R. Fuhrmann, C. Preza, J. A. O'Sullivan, D. L. Snyder, and W. H. Smith, "Spectrum estimation from quantum-limited interferograms," *IEEE Transactions on Signal Processing*, vol. 52, no. 4, pp. 950–961, 2004.
- [21] M. Donatelli and S. Serra-Capizzano, Eds., *Computational methods for inverse problems in imaging*. Springer-Verlag GmbH, 2019.
- [22] R. J. Bell, "Introductory Fourier transform spectroscopy," *American Journal of Physics*, vol. 41, no. 1, pp. 149–151, 1973.
- [23] H. E. Snell, W. B. Cook, and P. B. Hays, "Multiplex Fabry-Perot interferometer: II. Laboratory prototype," *Applied Optics*, vol. 34, no. 24, pp. 5268–5277, 1995.
- [24] Q. Yang, "Compact ultrahigh resolution interferometric spectrometer," *Optics Express*, vol. 27, no. 21, pp. 30606–30617, 2019.
- [25] Y.-C. Wang, L.-H. Shyu, and C.-P. Chang, "The comparison of environmental effects on Michelson and Fabry-Perot interferometers utilized for the displacement measurement," *Sensors*, vol. 10, no. 4, pp. 2577–2586, 2010.
- [26] P. Jacquinet, "The luminosity of spectrometers with prisms, gratings, or Fabry-Perot etalons," *Journal of the Optical Society of America*, vol. 44, no. 10, pp. 761–765, 1954.
- [27] S. Gousset, D. Picone, E. Le Coarer, J. Rodrigo, D. Voisin, L. Croize, Y. Ferrec, and M. Dalla Mura, "ImSPOC: A novel compact hyperspectral camera for the monitoring of atmospheric gases," in *IEEE International Geoscience and Remote Sensing Symposium (IGARSS)*. IEEE, 2022, pp. 5293–5296.
- [28] L.-J. Chen, T.-F. Kao, J.-Y. Lu, and C.-K. Sun, "A simple terahertz spectrometer based on a low-reflectivity Fabry-Perot interferometer using Fourier transform spectroscopy," *Optics Express*, vol. 14, no. 9, p. 3840, 2006.
- [29] M. Pisani and M. Zucco, "Compact imaging spectrometer combining Fourier transform spectroscopy with a Fabry-Perot interferometer," *Optics Express*, vol. 17, no. 10, pp. 8319–8331, 2009.
- [30] M. Zucco, V. Caricato, A. Egidi, and M. Pisani, "A hyperspectral camera in the UVA band," *IEEE Transactions on Instrumentation and Measurement*, vol. 64, no. 6, pp. 1425–1430, 2015.
- [31] R. Wright, M. Nunes, P. Lucey, S. Gunapala, D. Ting, C. Ferrari-Wong, L. Flynn, A. Soibel et al., "HYTI: High spectral resolution thermal imaging from a cubesat," in *IEEE International Geoscience and Remote Sensing Symposium (IGARSS)*. IEEE, 2022, pp. 7143–7145.
- [32] Y. Xu, J. Li, C. Bai, H. Yuan, and J. Liu, "Ultra-compact Fourier transform imaging spectrometer using a focal plane birefringent interferometer," *Optics Letters*, vol. 43, no. 17, pp. 4081–4084, 2018.
- [33] Q. Yang, "First order design of compact, broadband, high spectral resolution ultraviolet-visible imaging spectrometer," *Optics Express*, vol. 28, no. 4, p. 5587, Feb 2020.
- [34] T. A. Al-Saeed and D. A. Khalil, "Fourier transform spectrometer based on Fabry-Perot interferometer," *Applied Optics*, vol. 55, no. 20, p. 5322, Jul. 2016.
- [35] A. J. Jerri, "The Shannon sampling theorem—its various extensions and applications: A tutorial review," *Proceedings of the IEEE*, vol. 65, no. 11, pp. 1565–1596, 1977.
- [36] N. M. Gürel, K. Kara, A. Stojanov, T. Smith, T. Lemmin, D. Alistarh, M. Püschel, and C. Zhang, "Compressive sensing using iterative hard thresholding with low precision data representation: Theory and applications," *IEEE Transactions on Signal Processing*, vol. 68, pp. 4268–4282, 2020.
- [37] F. Wang, X. Tian, X. Liu, B. Gu, F. Zhou, and Y. Chen, "Combination complex-valued bayesian compressive sensing method for sparsity constrained deconvolution beamforming," *IEEE Transactions on Instrumentation and Measurement*, vol. 71, pp. 1–13, 2022.
- [38] H. Gupta, J. Fageot, and M. Unser, "Continuous-domain solutions of linear inverse problems with Tikhonov versus generalized TV regularization," *IEEE Transactions on Signal Processing*, vol. 66, no. 17, pp. 4670–4684, 2018.
- [39] P. Bohra and M. Unser, "Continuous-domain signal reconstruction using $l_{\{p\}}$ -norm regularization," *IEEE Transactions on Signal Processing*, vol. 68, pp. 4543–4554, 2020.
- [40] J. Idier, *Bayesian approach to inverse problems*. John Wiley & Sons, 2013.
- [41] M. Jouni, D. Picone, and M. Dalla Mura, "Model-based spectral reconstruction of interferometric acquisitions," in *IEEE International Conference on Acoustics, Speech, and Signal Processing (ICASSP)*. IEEE, 2023.
- [42] D. Picone, M. Jouni, and M. Dalla Mura, "Spectro-spatial hyperspectral image reconstruction from interferometric acquisitions," in *IEEE International Conference on Acoustics, Speech and Signal Processing (ICASSP)*. IEEE, 2024, pp. 2590–2594.
- [43] P. C. Hansen, "Truncated singular value decomposition solutions to discrete ill-posed problems with ill-determined numerical rank," *SIAM Journal on Scientific and Statistical Computing*, vol. 11, no. 3, pp. 503–518, 1990.
- [44] G. H. Golub, P. C. Hansen, and D. P. O'Leary, "Tikhonov regularization and total least squares," *SIAM Journal on Matrix Analysis and Applications*, vol. 21, no. 1, pp. 185–194, 1999.
- [45] I. Loris and C. Verhoeven, "On a generalization of the iterative soft-thresholding algorithm for the case of non-separable penalty," *Inverse Problems*, vol. 27, no. 12, p. 125007, 2011.
- [46] S. P. Boyd and L. Vandenberghe, *Convex optimization*. Cambridge university press, 2004.
- [47] R. Tibshirani, "Regression shrinkage and selection via the LASSO," *Journal of the Royal Statistical Society Series B: Statistical Methodology*, vol. 58, no. 1, pp. 267–288, 1996.
- [48] L. Condat, D. Kitahara, A. Contreras, and A. Hirabayashi, "Proximal splitting algorithms for convex optimization: A tour of recent advances, with new twists," *SIAM Review*, vol. 65, no. 2, pp. 375–435, may 2023.
- [49] A. Beck and M. Teboulle, "A fast iterative shrinkage-thresholding algorithm for linear inverse problems," *SIAM Journal on Imaging Sciences*, vol. 2, no. 1, pp. 183–202, 2009.
- [50] N. Parikh, S. Boyd et al., "Proximal algorithms," *Foundations and trends® in Optimization*, vol. 1, no. 3, pp. 127–239, 2014.



Mohamad Jouni (Member, IEEE) received the B.Eng. degree in Computer and Communications Engineering from the Lebanese University, Beirut, Lebanon, in 2016, and the M.Sc. and Ph.D. degrees in Signal and Image Processing from Grenoble Institute of Technology and the University of Grenoble Alpes, Grenoble, France, in 2017 and 2021 respectively. Since 2021, he has been a Postdoctoral Researcher at Grenoble Institute of Technology, Grenoble, France. In 2019 and 2023, he was a visiting researcher for 10 and 6 weeks, respectively, at Tokyo Institute of Technology, Tokyo, Japan. His interests include computational imaging, tensor algebra, hybrid AI methods, applications of multimodal and hyperspectral data analysis, and technology transfer.



Daniele Picone (Member, IEEE) received the B.Sc. and M.Sc. degrees in electronic engineering from the University of Salerno, Salerno, Italy, in 2008 and 2016, respectively, and the Ph.D degree in Signal and Image processing from the University of Grenoble Alpes, Grenoble, France, in 2021. In 2016, he was a Research fellow for 4 months at University of Salerno. In 2019, he was a visiting researcher at the Tokyo Institute of Technology, Japan for three months. Since December 2021, he was a Postdoctoral fellow for one year with the University of Grenoble Alpes, Grenoble, France, and then with the Grenoble Institute of Technology (Grenoble-INP), Grenoble, France, starting from January 2023. He is conducting his research at the Grenoble Images Speech Signals and Automatics Laboratory (GIPSA-Lab). His main research activities are in the fields of image processing and remote sensing, with applications mainly involving computational imaging, optimization, data fusion, and hyperspectral data processing.



Mauro Dalla Mura (Senior Member, IEEE) received the B.Sc. and M.Sc. degrees in Telecommunication Engineering from the University of Trento, Italy in 2005 and 2007, respectively. He obtained in 2011 a joint Ph.D. degree in Information and Communication Technologies (Telecommunications Area) from the University of Trento, Italy and in Electrical and Computer Engineering from the University of Iceland, Iceland. In 2011 he was a Research fellow at Fondazione Bruno Kessler, Trento, Italy, conducting research on computer vision. He is

currently an Assistant Professor at Grenoble Institute of Technology (Grenoble INP), France since 2012. He is conducting his research at the Grenoble Images Speech Signals and Automatics Laboratory (GIPSA-Lab). He is a Junior member of the Institut Universitaire de France (2021-2026). Dr. Dalla Mura has been appointed "Specially Appointed Associate Professor" at the School of Computing, Tokyo Institute of Technology, Japan for 2019-2022. His main research activities are in the fields of remote sensing, computational imaging, image and signal processing. Dr. Dalla Mura was the recipient of the IEEE GRSS Second Prize in the Student Paper Competition of the 2011 IEEE IGARSS 2011 and co-recipient of the Best Paper Award of the International Journal of Image and Data Fusion for the year 2012-2013 and the Symposium Paper Award for IEEE IGARSS 2014. Dr. Dalla Mura was the IEEE GRSS Chapter's Committee Chair for 2020-2021. He was President of the IEEE GRSS French Chapter 2016-2020 (he previously served as Secretary 2013-2016). In 2017 the IEEE GRSS French Chapter was the recipient of the IEEE GRSS Chapter Award and the "Chapter of the year 2017" from the IEEE French Section. He is on the Editorial Board of the IEEE Journal of Selected Topics in Applied Earth Observations and Remote Sensing (J-STARS) since 2016.